Ionic-Defect Distribution Revealed by Improved Evaluation of Deep-Level Transient Spectroscopy on Perovskite Solar Cells

Sebastian Reichert,[1,*] Jens Flemming,[2] Qingzhi An,[3,4] Yana Vaynzof,[3,4] Jan-Frederik Pietschmann,[2] and Carsten Deibel[1,†]

[1] *Institut für Physik, Technische Universität Chemnitz, Chemnitz 09126, Germany*

[2] *Fakultät für Mathematik, Technische Universität Chemnitz, Chemnitz 09126, Germany*

[3] *Kirchhoff-Institut für Physik and Center for Advanced Materials, Ruprecht-Karls-Universität Heidelberg, Im Neuenheimer Feld 227, Heidelberg 69120, Germany*

[4] *Technische Universität Dresden, Institut für Angewandte Physik and Center for Advancing Electronics Dresden (cfaed), Nöthnitzer Straße 61, Dresden 01069, Germany*

(Received 15 October 2019; revised manuscript received 19 December 2019; accepted 17 January 2020; published 6 March 2020)

One of the key challenges for the future development of efficient and stable metal-halide perovskite solar cells is related to the migration of ions in these materials. Mobile ions have been linked to the observation of hysteresis in the current-voltage characteristics, shown to reduce device stability against degradation and act as recombination centers within the band gap of the active layer. In the literature, one finds a broad spread of reported ionic defect parameters (e.g., activation energies) for seemingly similar perovskite materials, rendering the identification of the nature of these species difficult. In this work, we perform temperature-dependent deep-level transient spectroscopy (DLTS) measurements on methylammonium-lead-iodide perovskite solar cells and develop a extended regularization algorithm for inverting the Laplace transform. Our results indicate that mobile ions form a distribution of emission rates (i.e., a distribution of diffusion constants) for each observed ionic species, which may be responsible for the differences in the previously reported defect parameters. Importantly, different DLTS modes such as optical and current DLTS yield the same defect distributions. Finally, the comparison of our results with conventional boxcar DLTS and impedance spectroscopy verifies our evaluation algorithm.

DOI: 10.1103/PhysRevApplied.13.034018

I. INTRODUCTION

In recent years, solar cells based on organic-inorganic perovskite semiconductors have gained significant attention from the emerging photovoltaics community [1]. Perovskites exhibit many advantageous properties, such as high charge-carrier lifetimes, large absorption coefficients, and impressive power-conversion efficiencies [2–6]. However, perovskites are also rich in ionic defects, which have been shown to cause hysteresis and reduced stability [7–10]. Among the various types of native point defects in methylammonium-lead-iodide ($MAPbI_3$) perovskite, vacancies such as V_I^+ and V_{MA}^-, and interstitials such as I_i^- and MA_i^+ have been reported to be the most dominant ionic defects [11–16]. The iodine interstitial and the iodine vacancy, which can act as recombination centers [13,17], have been shown to be the most mobile species [15,18,19]. Unfortunately, a wide variation of different ionic defect parameters such as activation energies have been reported in the literature [11,14,18,20,21], even for the same types of perovskite solar cells. Therefore, the identification of the nature of these species is difficult. This is particularly noticeable for iodine migration. Theoretical calculations have predicted an activation energy of 0.1 eV for iodine migration [18]. Duan *et al.* [22] found an activation energy of 0.16 eV by admittance spectroscopy. A slightly higher activation energy was determined by transient ionic-drift measurements to 0.29 eV [11]. Chronophotoampereometry measurements have revealed activation energies of 0.6 eV [20]. Overall, the results reported in the literature for the activation energy of iodine ions vary within 0.5 eV.

In this work, we perform deep-level transient spectroscopy (DLTS) measurements to examine the properties of mobile ions in $MAPbI_3$ solar cells. The capacitance transients obtained by DLTS typically represent the response of a wide range of emission rates. The analysis of such multiexponential processes is challenging due to the commonly unknown number of single components. It is further complicated by the superposition of closely adjacent time

*sebastian.reichert@physik.tu-chemnitz.de

†deibel@physik.tu-chemnitz.de

constants in the presence of noise. Herein, we introduce an enhanced regularization algorithm for the inverse Laplace transform that significantly simplifies the evaluation of DLTS measurements. The application of this algorithm to temperature-dependent DLTS data reveals three distinct ionic species, each exhibiting a distribution of diffusion coefficients. A comparison with conventional boxcar evaluation verifies the results obtained by the regularization algorithm. Moreover, the results are consistent when different DLTS modes, such as reverse, optical, and current DLTS, are applied to obtain a more detailed understanding of the distributions of diffusion coefficients. Our measurements indicate two anion and one cation distributions, which we assign to I_i^-, V_{MA}^-, and MA_i^+, respectively. The diffusion coefficients of I_i^- and V_{MA}^- are found to be three orders of magnitude higher than that of the MA_i^+ species, indicating the high mobility of I_i^- and V_{MA}^- ions. The ion concentrations of all species are within the same order of magnitude, so that all species have a comparably high impact on the device properties. It is noteworthy that the observed ionic defect distributions can explain the large deviations of ionic defect parameters previously reported in the literature. Finally, unraveling these defect distributions can help us to understand how to avoid their formation during the active-layer fabrication, in order to improve the performance and stability of perovskite solar cells. Alternatively, it may assist with the development of passivation strategies tailored to certain types of defects.

II. METHODS AND THEORY

A. Sample preparation and current density–voltage characteristics

Prepatterned indium-tin-oxide- (ITO) coated glass substrates (PsiOTech Ltd., 15 Ω/sqr) are ultrasonically cleaned with 2% Hellmanex detergent, deionized water, acetone, and isopropanol, followed by 10 min of oxygen-plasma treatment. Modified poly(3,4-ethylenedioxythiophene):poly(styrenesulfonate) (m-PEDOT:PSS) is spin cast on the clean substrates at 4000 revolutions per minute (rpm) for 30 s and annealed at 150 °C for 15 min to act as a hole-transport layer [23]. The $MAPbI_3$ active layer is formed using the lead-acetate-trihydrate route following previous works [24,25]. In short, the perovskite solution (at a stoichiometry of 1:3.00 MAI:$PbAc_2$) is spin cast at 2000 rpm for 60 s in a dry air-filled glove box (relative humidity $< 0.5\%$). After blowing for 25 s and drying for 5 min, the as-spun films are annealed at 100 °C for 5 min, forming a uniform perovskite layer. The prepared samples are transferred to a nitrogen-filled glove box, where an electron-transport layer consisting of 20 mg ml^{-1} of [6,6]-phenyl-C61-butyric acid methylester ($PC_{60}BM$), dissolved in chlorobenzene, is dynamically spin cast at 2000 rpm for 30 s on the perovskite layer, followed by a 10 min annealing at 100 °C. Sequentially, a hole-blocking layer consisting of 0.5 mg ml^{-1} of bathocuproine (BCP), dissolved in isopropanol, is spin cast on top of the $PC_{60}BM$. The device is completed with a thermally evaporated 80-nm-thick silver layer.

The current density–voltage (j-V) characteristics are measured using a computer-controlled Keithley 2450 Source Measure Unit under simulated AM 1.5 sunlight with 100 mW cm^{-2} irradiation (Abet Sun 3000 Class AAA solar simulator). The light intensity is calibrated with a Si reference cell [National Institute of Standards and Technology (Gaithersburg, Md.) (NIST) traceable, VLSI] and corrected by measuring the spectral mismatch between the solar spectrum, the spectral response of the perovskite solar cell, and the reference cell.

B. Ionic defects in perovskite solar cells

Ionic defects have a major impact on device stability and performance and can lead to deep-level trapping of charge carriers [13,17,25–28]. It is therefore necessary to include the ionic responses when analyzing the solar-cell behavior. When describing the capacitance of a perovskite solar cell, the capacitive response caused by ions (C_{ion}) has to be added to the geometrical capacitance (C_0, considering the solar cells as classical parallel-plate capacitors dependent on the permittivity ϵ_R, the active area A, and the thickness L of the solar cell) and the capacitance caused by charge carriers trapped in defect states (C_{trap}):

$$C_{\mathrm{tot}} = C_0 + C_{\mathrm{trap}} + C_{\mathrm{ion}}. \tag{1}$$

As recent studies show, mobile ions are a dominant process for limiting device performance and stability. Classical semiconductor deep-level defects are less significant, because of the low concentration of such defects compared with the high concentration of mobile ionic species [11,28–30]. These results are confirmed by theoretical calculations and simulations showing that the deep-level trapping of charge carriers is quite unlikely compared to ionic movement [14,16,31,32]. Mobile ions must overcome an activation energy E_A in order to hop between localized states within the perovskite lattice [33–35]. A temperature-dependent emission rate e_t can be defined to describe this hopping process [11,36,37]:

$$e_t = \frac{e^2 D N_{\mathrm{eff}}}{k_B T \epsilon_0 \epsilon_R}, \tag{2}$$

where e is the elementary charge, D is the ion-diffusion coefficient, N_{eff} is the effective doping density, k_B is the Boltzmann constant, T is the temperature, and ϵ_0 the absolute dielectric permittivity. The ion-diffusion coefficient is

linked to the activation energy E_A by

$$D = D_0 \exp\left(-\frac{E_A}{k_B T}\right), \tag{3}$$

where D_0 is the diffusion coefficient at infinite temperatures.

C. Characterization of mobile ions with DLTS

An effective technique to obtain specific information about mobile ions in perovskite solar cells is DLTS [38]. This technique was originally conceived for measuring electronic deep-level defects but mobile ions can also be investigated due to their dependence on external voltages and capacitive response. The device under test is initially biased at zero volts. During a voltage or light pulse, mobile ions previously located at an interface between the perovskite layer and the transport layer are pushed into the perovskite until they reach a new steady state. After the pulse is finished, the mobile ions relax back to the steady-state condition by returning to the interfaces, which gives rise to a capacitance transient

$$C_t = C_\infty \pm \Delta C \exp\left(-e_t t\right), \tag{4}$$

where C_∞ is the steady-state capacitance. The ion concentration N_{ion} is proportional to ΔC:

$$\Delta C \propto \frac{N_{\text{ion}}}{N_{\text{eff}}} C_\infty, \quad \text{if } N_{\text{ion}} \ll N_{\text{eff}}. \tag{5}$$

The DLTS setup used in this work consists of a Zurich Instruments MFLI lock-in amplifier with MF-IA and MF-MD options, a Keysight Technologies 33600A function generator, and a Janis ST500 cryoprobe station with a Lakeshore 336 temperature controller. The capacitance transients (Fig. 1) are recorded in the temperature range of 200 K to 350 K, in 5 K steps, controlled accurately to within 0.01 K, using liquid nitrogen for cooling. The DLTS measurements are performed using an ac frequency of 80 kHz with an amplitude of $V_{\text{ac}} = 20$ mV and biasing the perovskite device from 0 V to 1 V for 100 ms. The transients are measured over 30 s and averaged over 35 single measurements.

Several methods are available for the extraction of characteristic information from DLTS data. Most commonly, DLTS is evaluated using the boxcar method [38–40]. Plotting the extracted emission rates on logarithmic scale over $1000/T$ in an Arrhenius diagram results in straight lines according to Eq. (9). These straight lines contain information about the activation energy for ion migration (the slope) and for the diffusion coefficient (the y intercept). Boxcar evaluation is a valuable technique to obtain emission rates without presuming any specific model. The disadvantage of boxcar evaluation is the low time resolution, especially in the presence of noise, which makes it difficult to distinguish between two closely spaced rates (see Sec. I of the Supplemental Material [41]). A more sensitive evaluation method is achieved by the inverse Laplace transform. The exponential capacitance transient $C(t)$ can be considered as the Laplace transform of a function in the transform space e_t [42,43]. This means that $C(t)$ is the Laplace transform of $g(e_t)$ and can be expressed as follows:

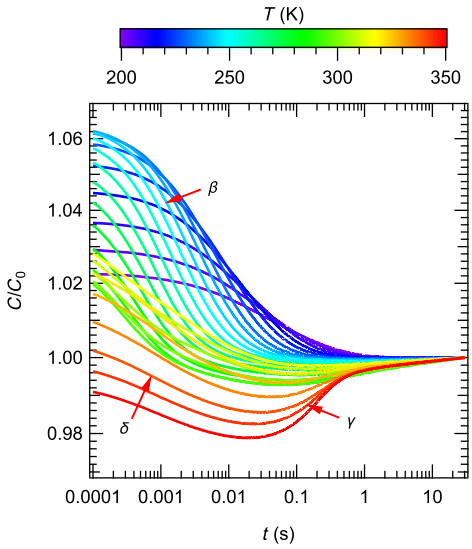

FIG. 1. The DLTS measurements on a $MAPbI_3$ solar cell for different temperatures from 200 K to 350 K, in 5 K steps. The capacitance transients are obtained after pulsing the sample from 0 V to 1 V for 100 ms.

$$C(t) = \sum_i C_i \exp\left(-e_{t_i} t\right) = \int_0^\infty g(e_t) \exp\left(-e_t t\right) de_t. \tag{6}$$

The inverse Laplace transform of $C(t)$ is subsequently given by the spectral function $g(e_t)$:

$$g(e_t) = \sum_i C_i \delta(e_t - e_{t_i}). \tag{7}$$

Peaks at $e_t = e_{t_i}$ can be obtained by plotting $g(e_t)$ versus e_t and by transferring the emission rates into an Arrhenius diagram according to Eq. (9).

Since inverting the Laplace transform is an ill-posed problem in the sense that small errors in measurements may yield large errors in the inversion, regularization of the inversion process is necessary. A first numerical implementation was developed by Provencher [44] (CONTIN) and later modified (FTIKREG) [44–48]. In order to use these Tikhonov regularization–based methods successfully, a high signal-to-noise ratio (SNR) in the range of 1000 is required [48]. A large number of transients have to be averaged to achieve such a high SNR. This issue is challenging

because of the long transient time of about 30 s that is necessary for measuring ion movement in perovskite solar cells. The long recording time in combination with averaging over a high number of single measurements for each transient would result in long measurement times for each temperature step. To overcome this issue, we implement an improved algorithm to regularize the inverse Laplace transform, implemented in the modern programming language PYTHON. The enhanced method is fast and easy in use due to the reduced amount of parameters needed to achieve reliable results.

D. Numerical inversion of Laplace transform via regularized sparse Laplace spectrum REGSLAPS

Inversion of the Laplace transform in Eq. (6) is an ill-posed problem in the sense that very small deviations in the data C (noise, round-off errors) may cause extremely large errors in the solution g. Equivalently, very different spectral functions g may have almost the same Laplace transform and, thus, cannot be reconstructed solely from data C, as the very small difference between their Laplace transforms cannot be distinguished from noise.

To obtain reasonable reconstruction results for ill-posed problems, additional information about expected solutions has to be taken into account. One standard approach is Tikhonov's regularization method:

$$\|L\,g - C\|^2 + \alpha\|g\|^2 \to \min_g . \tag{8}$$

Here, $\|\cdot\|$ denotes the mean-square norm of a function and L is the Laplace transform, a linear mapping. The regularization parameter $\alpha > 0$ controls the trade-off between data fitting and regularization, where the latter is a consequence of the penalty term $\|g\|^2$. For details on Tikhonov regularization, see Engl *et al.* [49].

Additional information added by this standard Tikhonov approach is that the sought-for spectral function has a small norm. The CONTIN algorithm for processing DLTS measurements uses the squared norm of the second derivative g'' as a penalty instead of $\|g\|^2$. This leads to very smooth (low-curvature) spectral functions g. The advantage of the CONTIN approach is that its numerical realization is rather simple, since minimization of the corresponding Tikhonov-like functional is achieved by simply solving a well-posed system of linear equations.

The approach presented here differs significantly from standard Tikhonov and CONTIN. Since, in addition to smooth sections, Laplace spectra may also contain sharp peaks, it is undesirable to apply methods that yield only very smooth results. Deciding whether a smooth regularized spectrum originates from sharp peaks or from smooth distributions is almost impossible. But, as is shown in Sec. III, starting from a regularized spectrum containing peaks, it can easily be determined whether the real spectrum is smooth or contains peaks.

Functions consisting of a small number of peaks can be mathematically encoded as preferring a function that is zero over large parts of its domain. Such functions are the usual outcome of a method called ℓ^1 regularization (see Daubechies *et al.* [50]). This method involves solving the minimization problem

$$\|L\,g - C\|^2 + \alpha \int_0^\infty |g(e_t)|\,de_t \to \min_g .$$

The problem is again of Tikhonov type but is accompanied by a nondifferentiable penalty due to the absolute value inside the integral. This nondifferentiability makes numerical minimization more challenging.

Our implementation REGSLAPS is based on a fast iterative soft-threshold algorithm (FISTA) [51], which is essentially a projected gradient method. To describe the algorithm, we replace the spectral function g by a finite vector of function values at fixed grid points. Then, the Laplace transform L becomes a matrix that maps g to a finite data vector C. We use the following algorithm:

(a) $\alpha > 0$ (details below), set g to zero everywhere, set $g_{\text{old}} := g$
(b) Do until convergence:
  (i) Mixing step: $g_{\text{mix}} := g + [(i-1)/(i+2)]\,(g - g_{\text{old}})$ (where i is the iteration counter)
  (ii) Calculate gradient of fitting functional: $d := L^T\,(L\,g_{\text{mix}} - C)$
  (iii) Calculate step size: $s := \|d\|^2/\|L\,d\|^2$
  (iv) Gradient step: $\tilde{g} := g_{\text{mix}} - s\,d$
  (v) Projection step: for all k, set $g_{\text{proj}} := (\text{sign}\,\tilde{g}_k)\,\max\{0,\ |\tilde{g}_k| - s\,\alpha\}$
  (vi) Update: set $g_{\text{old}} := g$ and $g := g_{\text{proj}}$

The choice of the regularization parameter α is crucial and difficult. However, DLTS data are very smooth for prolonged times t, which allows us to obtain a reasonable estimate for the data's noise level as the difference between the measured data and a smoothed version of the measured data. Based on this noise level, we can apply Morozow's discrepancy principle [52] as follows:

(a) Choose some large initial α.
(b) Calculate the regularized solution, denoted by g_α.
(c) Do until $\|L\,g_\alpha - C\| \le k\eta$ (where η is the noise level and $k > 1$ a constant close to one):
  (i) Decrease α by some fixed factor.
  (ii) Calculate regularized solution g_α.
(d) The last g_α is the result of the method.

The estimate of the spectral function g allows for peaks to be simply identified as the grid points for which g is not

zero. Tests using synthetic data confirm that the area under the curve is very close to the height of a δ peak in the exact spectral function. For a verification of our algorithm, we try to reproduce the prefactor and time constants of several synthetic multiexponential decays (see Sec. I of the Supplemental Material [41]). In all cases, REGSLAPS is able to reproduce the parameters of the synthetic data accurately. This approach serves as a test of the validity of REGSLAPS.

III. RESULTS AND DISCUSSION

The photovoltaic performance of the devices investigated here is that of typical $MAPbI_3$ solar cells. The current density–voltage characteristics are shown in part II of the Supplemental Material [41]. The device exhibits a current density of 21.6 mA cm^{-2}, an open-circuit voltage of 0.96 V, a fill factor of 76.5%, and a power-conversion efficiency of 15.8%. As reported in the literature, j-V measurements are often affected by hysteresis [53–55]. The origin of hysteresis is attributed to mobile ions within the active layer of perovskite solar cells [56–59]. The j-V data show almost no hysteresis but, corresponding to the results of Calado *et al.* [60], ion migration can also take place in devices with minimal hysteresis.

In Sec. III of the Supplemental Material [41], the rate-window evaluation of the DLTS transients (Fig. 1) is shown. Three ion-related peaks are visible, which are labeled as β, γ, and δ. The signs of the peaks are related to the charge state of the contributing ions. Defects β and δ are anions, whereas γ is a cation. We determine that the two low-frequency responses below 10 Hz correspond to the same defect γ. We cannot exclude the possibility that the defects β and δ correspond to the same ionic origin. However, as a working hypothesis, we assume that they are different ionic defects, as we do not observe a change in the activation energy or diffusion coefficient according to Futscher *et al.* [11] in the IS data at the tetragonal-cubic phase-transition temperature at 327 K [61].

We distinguish the nature of defects—electronic or ionic—by applying reverse DLTS [62,63]. In this technique, the filling pulse is reversed, meaning that the voltage pulse goes from 1 V to 0 V. Other parameters such as the ac frequency and the filling-pulse parameters remain constant. As a consequence for electronic traps, the capture process of charge carriers in trap states is measured in contrast to conventional DLTS measurements. Since the emission rate is much lower than the capture rate, the latter (determined by reverse DLTS) is expected to be higher than the emission rate (obtained by conventional DLTS) if deep-level trap states are being measured. The situation is different when mobile ions respond to the voltage pulse. When no external voltage is applied, mobile ions are at equilibrium at the interfaces of the perovskite layer due to the internal field [11,13]. As a result, the mobile ions will be pushed into the perovskite layer by the voltage pulse.

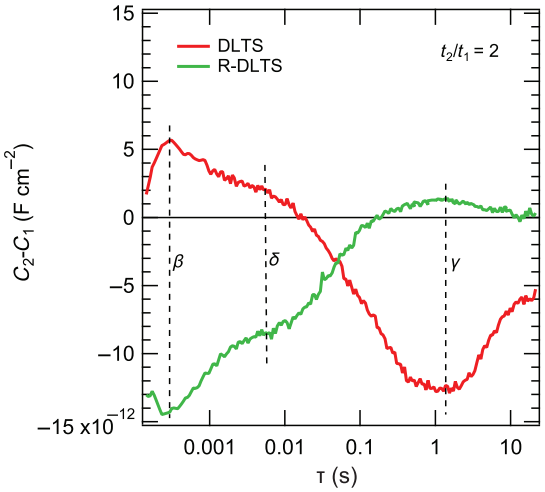

FIG. 2. Conventional DLTS and reverse DLTS evaluation via boxcar at room temperature with a rate window of $t_2/t_1 = 2$. The emission rates are equal for all defects, which indicates the underlying ionic origin.

For ions, it can be expected that this process is approximately as fast as the back drift of the ions to the interfaces. We measure reverse DLTS at room temperature and plot the boxcar evaluation for a rate window of $t_2/t_1 = 2$ in Fig. 2. Since the emission rates for all defects are comparable for conventional and reverse DLTS, we can conclude that the measured emission rates originate from mobile ions and not charge carriers such as electron and holes.

A defect signature can be obtained by measuring the emission rate $e_t(T)$ at different temperatures, as the emission rate for ions is thermally activated according to Eqs. (2) and (3) [11,18,21]:

$$e_t = \frac{e^2 N_{\text{eff}} D_0}{k_B T \epsilon_0 \epsilon_R} \exp\left(-\frac{E_A}{k_B T}\right). \tag{9}$$

Emission rates for each temperature, obtained by evaluating the peaks visible in the rate-window plot (see Sec. III of the Supplemental Material [41]), are plotted in Fig. 4. Equation (9) is used to fit the data, in order to determine the activation energy E_A and diffusion coefficient D with Eq. (3). For calculation of these defect parameters, the effective doping density and permittivity are determined by capacitance-voltage measurements (see Sec. IV of the Supplemental Material [41]) and the solar cells are prebiased at 1 V for 60 s and rapidly swept with 3 V s^{-1} in the reverse direction [64]). The results are summarized in Table I. We determine that the activation energy is 0.37 eV for β, 0.37 eV for γ, and 0.19 eV for δ. These results are in agreement with the results of Park *et al.* [19] and Yin *et al.* [14], which supports our findings that the measured ionic defects have low activation energies. The diffusion coefficient at 300 K for δ is determined to be 5×10^{-9} cm^2 s^{-1}. For β, the diffusion coefficient

TABLE I. The activation energy E_A, diffusion coefficient $D_{300\,\mathrm{K}}$ at 300 K, and ion concentration N_{ion} obtained by boxcar evaluation.

Defect	Ion	E_A (eV)	$D_{300\,\mathrm{K}}$ ($\mathrm{cm^2\,s^{-1}}$)	N_{ion} ($\mathrm{cm^{-3}}$)
β	V_{MA}^-	0.37	2×10^{-7}	6×10^{14}
γ	MA_i^+	0.37	1×10^{-11}	2×10^{14}
δ	I_i^-	0.19	5×10^{-9}	9×10^{13}

at 300 K is 2×10^{-7} $\mathrm{cm^2\,s^{-1}}$, which is several orders of magnitude higher when compared to that of γ, with 1×10^{-11} $\mathrm{cm^2\,s^{-1}}$. The determined diffusion coefficients at 300 K are in the range of 10^{-7}–10^{-12} $\mathrm{cm^2\,s^{-1}}$, consistent with values reported in literature [11,15,20,65,66]. The ion concentrations are found to be 6×10^{14} $\mathrm{cm^{-3}}$ for β, 2×10^{14} $\mathrm{cm^{-3}}$ for γ, and 9×10^{13} $\mathrm{cm^{-3}}$ for δ.

By comparison with the literature, we make a conceivable scenario for identifying the measured defects with mobile species in perovskite solar cells. First, we compare the results of our measurements with those reported by Futscher *et al.* [11] (see Sec. V of the Supplemental Material [41]). This allows us to attribute defect γ to MA_i^+, since both the position and the sign of both measurements are in good agreement. However, in contrast to the interpretation of phase-transition-induced changes of the diffusion coefficient and activation energy, our results predict that different parts of the same defect distribution are measured. This is in agreement with the two measured MA_i^+ responses determined by Futscher *et al.* [11] (see Sec. V, C1 and C2, of the Supplemental Material [41]), which belong to the same defect distribution. The identification of β and δ is less certain. The defect attributed to I_i^- (see Sec. V, A1, of the Supplemental Material [41]), measured by Futscher *et al.* [11], is indeed close to the edge of distribution β. However, both distribution β and distribution δ are very close to one another and the possibility that the distribution δ is also present at low temperatures and frequencies cannot be excluded. Consequently, the identification of β and δ is not possible by comparing with the results of Futscher *et al.* [11]. Instead, we compare our results with the DFT calculations of Yang *et al.* [21]. The reported activation energy of MA_i^+ ions (*a*-*b* plane, 0.38 eV; *c* axis, 0.48 eV) is in good agreement with our findings. Furthermore, the reported diffusion barrier of Yang *et al.* [21] for I_i^- ions (*a*-*b* plane, 0.19 eV; *c* axis, 0.33 eV) is in the same range as our result for defect δ. Therefore, we attribute δ to I_i^-. Since the only negative ion among all the likely native point defects left is V_{MA}^-, we assign β to V_{MA}^-. Noticeably, the activation energy of Yang *et al.* [21] for V_{MA}^- (*a*-*b* plane, 0.62 eV; *c* axis, 0.89 eV) does not agree with our findings and at the moment we do not yet have an explanation for that discrepancy. Moreover, we would expect comparable diffusion coefficients for both MA_i^+ and V_{MA}^-, in contrast to our observations (Table I). However, our assignment is in good agreement with the high mobility reported for anions, which is significantly higher than the mobility of cations [12,15,16,18,19].

It is important to note that the emission rates obtained by boxcar evaluation for β, γ, and δ cannot describe the capacitance transients completely. As shown in Fig. 3(a), we highlight this observation using the 230-K capacitance transient up to 0.1 s, which is exemplary for β. We choose this particular transient as a compromise between a good SNR and the absence of the response of the other defects, γ andδ. The monoexponential decay with the emission rate obtained by boxcar evaluation is insufficient to fit the experimental data. The ambiguity between the experimental result and the capacitance transient reconstructed very likely indicates a defect distribution, as a distribution of emission rates is necessary to describe the experimental transient. Consequently, by fitting a defect distribution consisting of two Gaussian distributions to the capacitance transient, which yields the emission-rate spectrum in Fig. 3(b), good agreement with the experimental capacitance transient can be obtained. The presence of a defect distribution would offer a reasonable explanation for the different and partly inconsistent defect parameters reported for perovskite solar cells in the literature [11,13,18,20,67]. Different experimental methods and conditions could lead

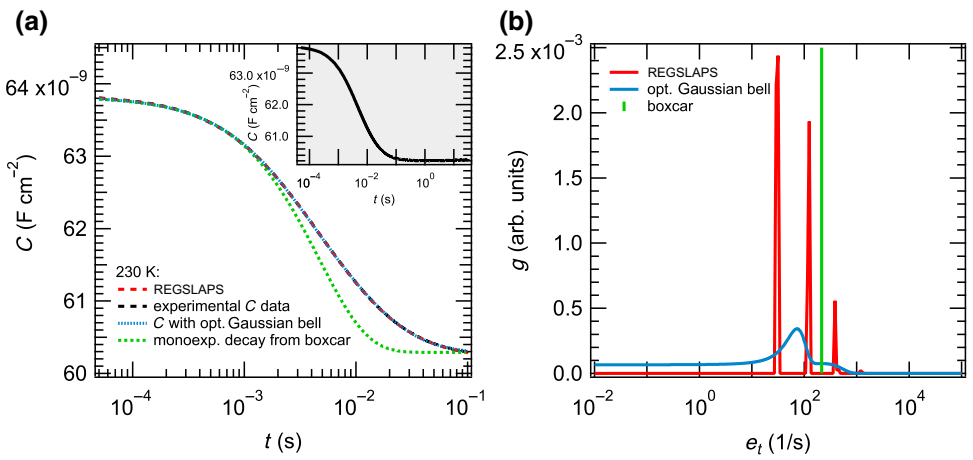

FIG. 3. (a) Capacitance transients of the experimental data, reconstructed with the emission rates calculated using REGSLAPS and reconstructed by fitting Gaussian defect distributions. The data are cut at 0.1 s to avoid the influence of γ on the fitting of Gaussian distributions to the emission-rate spectrum, which is still present even for low temperatures (inset). (b) The calculated emission-rate spectrum of REGSLAPS with a fit of the Gaussian distributions.

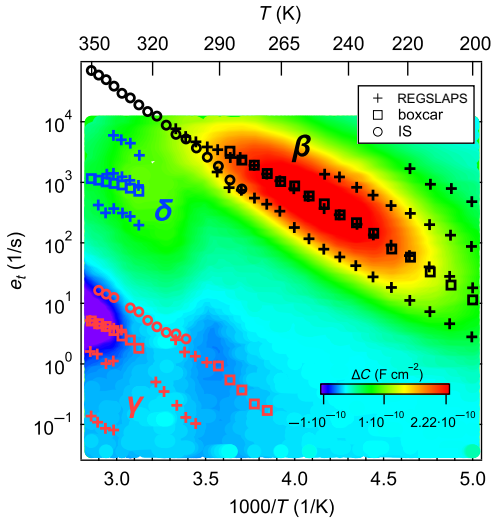

FIG. 4. A comparison of the emission rates obtained by conventional boxcar evaluation (contour plot in Sec. III of the Supplemental Material [41]), by inverse Laplace transform via REGSLAPS, and by impedance spectroscopy (IS). Three different ionic defects, β, γ, and δ, are visible. The parallel straight lines are related to ionic distributions.

to probing different parts of the defect distribution. We propose that the broad distribution of ionic defects might originate from the nonconstant internal electric field in perovskite solar cells, in part caused by ion migration.

To exploit the higher resolution offered by inverse Laplace transform, we use our REGSLAPS algorithm as described in Sec. D. At first, we again consider the example shown in Fig. 3. With REGSLAPS, we obtain three different sharp peaks, which are roughly equidistantly spaced [see Fig. 3(b)]. As shown in Fig. 3(a), the three sharp emission rates given by REGSLAPS, as well as the distribution of emission rates, are able to fit the data adequately. This means that we cannot distinguish whether the defect distribution or the emission rates given by REGSLAPS are more suitable for explaining the experimental result. The reason is that the inverse Laplace transform is an ill-posed problem. However, we test REGSLAPS with a synthetic Gaussian distribution and obtain equidistant peaks instead of the defect distribution in the resultant spectra (see Sec. I of the Supplemental Material [41]). This indicates that the measured emission rates with equidistant spacing correspond to a defect distribution. To achieve short calculation times, the algorithm described in Sec. II is adjusted to keep the number of calculated solutions small by preferring zeros in the solution space. Therefore, the emission-rate spectrum calculated using REGSLAPS results in e_t with equidistant spacing, instead of a continuous distribution of emission rates. Moreover, it has recently been reported that the perovskite-crystal grain orientation influences the rate of lateral ionic transport in spin-cast $MAPbI_3$ films [68]. In this work, photoluminescence microscopy was utilized to track the migration of ions upon the application of an electric field, with the results showing a broad quenching front being present only for films with a random grain orientation. Modeling of these results is only possible using a large distribution of diffusion coefficients for the same ionic defect. It is thus possible that different grain orientations in the vertical solar-cell devices also result in a wide distribution of ionic transport rates, in agreement with the results presented here. In summary, based on, first, the fact that our transient data cannot be reproduced with monoexponential decays, second, that REGSLAPS will yield distinct equally spaced rates when a distribution of rates is present, and, third, the information from Fassl *et al.* [68], in which the data can only be explained by a distribution of diffusion coefficients, we expect that all of our observed ion-migration rates belong to broad distributions.

With this finding, we evaluate the capacitance transients from Fig. 1 and plot the resulting emission rates in Sec. VI of the Supplemental Material [41]. As mentioned above, inverse Laplace transform is an ill-posed problem, so that artifacts can occur within the spectrum calculated using REGSLAPS. This means that only calculated emission rates that follow the emission-rates equation (9) are physically justifiable. Emission rates that satisfy this criterion are shown in Fig. 4, resulting in a set of straight lines for each defect. As discussed above, the emission rates that differ in the vertical offset are linked to a defect distribution.

The contour plot of the boxcar data (see Sec. III of the Supplemental Material [41]) in Fig. 4 shows excellent agreement with the equidistantly spaced emission rates, since all of the emission rates determined using REGSLAPS are within the bounds of the broad peak obtained by the boxcar evaluation. Only the maxima of the emission-rate peaks can be extracted by boxcar and are likely close to the peak of the experimental emission-rate distribution. The agreement between our algorithm REGSLAPS and the established but less sensitive boxcar evaluation also confirms the validity of REGSLAPS.

To verify our results, we perform impedance-spectroscopy (IS) measurements (see Sec. VII of the Supplemental Material [41]), which are analyzed and added to the contour plot (Fig. 4). As IS is a small-signal technique, the perovskite solar cells are closer to equilibrium conditions during the measurement compared with DLTS, where voltage pulses have a strong effect on the internal electric fields that influence the ion migration. The comparison of IS with DLTS is therefore very helpful to verify the results obtained by DLTS. As shown in Fig. 4, there is good agreement of the emission rates of defect β, whereas defect δ is not visible. In the case of defect γ, only one part of the defect distribution can be measured, in contrast to DLTS, because of the lower sensitivity of IS for low emission rates.

Additionally to the capacitance DLTS measurements (Fig. 1), we use different DLTS modes such as optical

DLTS (O-DLTS; see Sec. VIII of the Supplemental Material [41]) and current DLTS (I-DLTS; see Sec. IX of the Supplemental Material [41]) to verify our previous results and to learn more about the nature of these ionic defects. For O-DLTS, the solar cell is probed using a light pulse (250 $\mathrm{mW\,cm^{-2}}$ for 100 ms) instead of a voltage pulse. In the case of the I-DLTS measurements, the current response of the solar cells after applying the voltage pulse is measured simultaneously with the capacitance transient. Parameters such as the filling-pulse duration, the transient measurement time, and the number of averages correspond to those of capacitance DLTS. As shown in Sec. X of the Supplemental Material [41], all DLTS modes give access to the same defect distributions, whereas with each DLTS mode another part of the distribution is measurable. In the case of our I-DLTS measurements, more than one component of the defect distribution of γ and δ is visible, even in the boxcar evaluation, due to the higher resolution of I-DLTS measurements for higher emission rates in comparison to C-DLTS measurements. This verifies our result on the ionic defect distributions using REGSLAPS. The existence of transients in O-DLTS measurements indicates the ion movements caused by light interaction, since light induces free charge carriers with impact on the internal electrical field [20]. The result indicates the implication of mobile ions in optoelectronic measurements. Since mobile ions have an impact on the internal electrical field, they may influence the charge-carrier extraction and recombination in the perovskite solar cell. Moreover, an additional ionic response can occur, which can be mistakenly interpreted as an extraction or recombination rate. This must be taken into account for optoelectronic measurements such as intensity-modulated photocurrent spectroscopy (IMPS) and intensity-modulated photovoltage spectroscopy (IMVS), photocurrent-decay, and photovoltage-decay measurements [20,56,60,69–72].

IV. CONCLUSIONS

In this work, we perform DLTS measurements on $MAPbI_3$ perovskite solar cells and analyze them using an extended algorithm for inverse Laplace transform. Our results indicate the presence of three different mobile ions, which we attribute to V_{MA}^{-}, MA_i^{+}, and I_i^{-}, respectively. We introduce a improved numerical implementation of the regularization algorithm REGSLAPS for performing the inverse Laplace transform. Our algorithm is a powerful instrument for the evaluation of any kind of exponential decay and is especially useful to extract components of DLTS transients. By using REGSLAPS, we find that all measured mobile ions correspond to distributions of diffusion constants. This result could be the explanation for the different ionic defect parameters as reported in the literature. A range of different DLTS modes, as well as IS, verifies our findings.

Future developments in the field of perovskite solar cells depend on a detailed understanding of the ionic transport mechanisms and the degradation pathways influenced by ionic species. Our method and experimental results open routes for improvements in the fabrication process of perovskite solar cells in order to decrease the density of mobile ions within the active layer. Since the defect landscape may depend on the sample-preparation conditions, a continuation of this study should also include the dependence of the defect parameters on the fabrication parameters, such as the precursor solution stoichiometry.

ACKNOWLEDGMENTS

C.D. and S.R. acknowledge financial support by the Bundesministerium für Bildung und Forschung (BMBF Hyper project, Contract No. 03SF0514C) and thank their project partners from the University of Würzburg and ZAE Bayern for interesting discussions. Y.V. and C.D. thank the DFG for generous support within the framework of the SPP 2196 project (PERFECT PVs). We also thank Aron Walsh for his feedback concerning the interpretation of the ionic species.

S.R. and J.F. contributed equally to this work.

[1] P. K. Nayak, S. Mahesh, H. J. Snaith, and D. Cahen, Photovoltaic solar cell technologies: Analysing the state of the art, Nat. Rev. Mater. **4**, 269 (2019).

[2] A. M. A. Leguy, P. Azarhoosh, M. I. Alonso, M. Campoy-Quiles, O. J. Weber, J. Yao, D. Bryant, M. T. Weller, J. Nelson, A. Walsh, M. van Schilfgaarde, and P. R. F. Barnes, Experimental and theoretical optical properties of methylammonium lead halide perovskites, Nanoscale **8**, 6317 (2016).

[3] A. S. Chouhan, N. P. Jasti, S. Hadke, S. Raghavan, and S. Avasthi, Large grained and high charge carrier lifetime $CH_3NH_3PbI_3$ thin-films: Implications for perovskite solar cells, Curr. Appl. Phys. **17**, 1335 (2017).

[4] NREL, Best research-cell efficiency chart, https://www.nrel.gov/pv/cell-efficiency.html, accessed January 14, 2020.

[5] Q. Jiang, Z. Chu, P. Wang, X. Yang, H. Liu, Y. Wang, Z. Yin, J. Wu, X. Zhang, and J. You, Planar-structure perovskite solar cells with efficiency beyond 21%, Adv. Mater. **29**, 1703852 (2017).

[6] A. Polman, M. Knight, E. C. Garnett, B. Ehrler, and W. C. Sinke, Photovoltaic materials: Present efficiencies and future challenges, Science **352**, 6283 (2016).

[7] D. A. Jacobs, Y. Wu, H. Shen, C. Barugkin, F. J. Beck, T. P. White, K. Weber, and K. R. Catchpole, Hysteresis phenomena in perovskite solar cells: The many and varied effects of ionic accumulation, Phys. Chem. Chem. Phys. **19**, 3094 (2017).

[8] B. Rivkin, P. Fassl, Q. Sun, A. D. Taylor, Z. Chen, and Y. Vaynzof, Effect of ion migration-induced electrode degradation on the operational stability of perovskite solar cells, ACS Omega **3**, 10042 (2018).

[9] C. Li, S. Tscheuschner, F. Paulus, P. E. Hopkinson, J. Kießling, A. Köhler, Y. Vaynzof, and S. Huettner, Iodine migration and its effect on hysteresis in perovskite solar cells, Adv. Mater. **28**, 2446 (2016).

[10] N. Tessler and Y. Vaynzof, Preventing hysteresis in perovskite solar cells by undoped charge blocking layers, ACS Appl. Energy Mater. **1**, 676 (2018).

[11] M. H. Futscher, J. M. Lee, L. McGovern, L. A. Muscarella, T. Wang, M. I. Haider, A. Fakharuddin, L. Schmidt-Mende, and B. Ehrler, Quantification of ion migration in $CH_3NH_3PbI_3$ perovskite solar cells by transient capacitance measurements, Mater. Horiz. **6**, 1497 (2019).

[12] D. Meggiolaro, S. G. Motti, E. Mosconi, A. J. Barker, J. Ball, C. A. R. Perini, F. Deschler, A. Petrozza, and F. D. Angelis, Iodine chemistry determines the defect tolerance of lead-halide perovskites, Energy Environ. Sci. **11**, 702 (2018).

[13] D. Meggiolaro, E. Mosconi, and F. D. Angelis, Formation of surface defects dominates ion migration in lead-halide perovskites, ACS Energy Lett. **4**, 779 (2019).

[14] W.-J. Yin, T. Shi, and Y. Yan, Unusual defect physics in $CH_3NH_3PbI_3$ perovskite solar cell absorber, Appl. Phys. Lett. **104**, 063903 (2014).

[15] A. Senocrate, I. Moudrakovski, G. Y. Kim, T.-Y. Yang, G. Gregori, M. Grätzel, and J. Maier, The nature of ion conduction in methylammonium lead iodide: A multimethod approach, Angew. Chem. Int. Ed. **56**, 7755 (2017).

[16] A. Senocrate, T.-Y. Yang, G. Gregori, G. Y. Kim, M. Grätzel, and J. Maier, Charge carrier chemistry in methylammonium lead iodide, Solid State Ionics **321**, 69 (2018).

[17] M. H. Du, Efficient carrier transport in halide perovskites: Theoretical perspectives, J. Mater. Chem. A **2**, 9091 (2014).

[18] J. M. Azpiroz, E. Mosconi, J. Bisquert, and F. D. Angelis, Defect migration in methylammonium lead iodide and its role in perovskite solar cell operation, Energy Environ. Sci. **8**, 2118 (2015).

[19] J.-S. Park, J. Calbo, Y.-K. Jung, L. D. Whalley, and A. Walsh, Accumulation of deep traps at grain boundaries in halide perovskites, ACS Energy Lett. **4**, 1321 (2019).

[20] C. Eames, J. M. Frost, P. R. F. Barnes, B. C. O'Regan, A. Walsh, and M. S. Islam, Ionic transport in hybrid lead iodide perovskite solar cells, Nat. Commun. **6**, 7497 (2015).

[21] D. Yang, W. Ming, H. Shi, L. Zhang, and M.-H. Du, Fast diffusion of native defects and impurities in perovskite solar cell material $CH_3NH_3PbI_3$, Chem. Mater. **28**, 4349 (2016).

[22] H.-S. Duan, H. Zhou, Q. Chen, P. Sun, S. Luo, T.-B. Song, B. Bob, and Y. Yang, The identification and characterization of defect states in hybrid organic-inorganic perovskite photovoltaics, Phys. Chem. Chem. Phys. **17**, 112 (2015).

[23] C. Zuo and L. Ding, Modified PEDOT layer makes a 1.52 V V_{oc} for perovskite/PCBM solar cells, Adv. Energy Mater. **7**, 1601193 (2016).

[24] Q. An, Q. Sun, A. Weu, D. Becker-Koch, F. Paulus, S. Arndt, F. Stuck, A. S. K. Hashmi, N. Tessler, and Y. Vaynzof, Perovskite photovoltaic devices: Enhancing the open-circuit voltage of perovskite solar cells by up to 120 mV using π-extended phosphoniumfluorene electrolytes as hole blocking layers, Adv. Energy Mater. **9**, 1970126 (2019).

[25] P. Fassl, V. Lami, A. Bausch, Z. Wang, M. T. Klug, H. J. Snaith, and Y. Vaynzof, Fractional deviations in precursor stoichiometry dictate the properties, performance and stability of perovskite photovoltaic devices, Energy Environ. Sci. **11**, 3380 (2018).

[26] Y. Zhao, W. Zhou, H. Tan, R. Fu, Q. Li, F. Lin, D. Yu, G. Walters, E. H. Sargent, and Q. Zhao, Mobile-ion-induced degradation of organic hole-selective layers in perovskite solar cells, J. Phys. Chem. C **121**, 14517 (2017).

[27] S. Kim, S. Bae, S.-W. Lee, K. Cho, K. D. Lee, H. Kim, S. Park, G. Kwon, S.-W. Ahn, H.-M. Lee, Y. Kang, H.-S. Lee, and D. Kim, Relationship between ion migration and interfacial degradation of $CH_3NH_3PbI_3$ perovskite solar cells under thermal conditions, Sci. Rep. **7**, 1200 (2017).

[28] Y. Cheng, H.-W. Li, J. Qing, Q.-D. Yang, Z. Guan, C. Liu, S. H. Cheung, S. K. So, C.-S. Lee, and S.-W. Tsang, The detrimental effect of excess mobile ions in planar $CH_3NH_3PbI_3$ perovskite solar cells, J. Mater. Chem. A **4**, 12748 (2016).

[29] J. H. Song, X. D. Mai, S. Jeong, and Y.-H. Kim, Hysteresis and photoinstability caused by mobile ions in colloidal quantum dot photovoltaics, J. Phys. Chem. Lett. **8**, 5259 (2017).

[30] T. S. Sherkar, C. Momblona, L. Gil-Escrig, J. Ávila, M. Sessolo, H. J. Bolink, and L. J. A. Koster, Recombination in perovskite solar cells: Significance of grain boundaries, interface traps, and defect ions, ACS Energy Lett. **2**, 1214 (2017).

[31] A. Buin, R. Comin, J. Xu, A. H. Ip, and E. H. Sargent, Halide-dependent electronic structure of organolead perovskite materials, Chem. Mater. **27**, 4405 (2015).

[32] Y. Rakita, I. Lubomirsky, and D. Cahen, When defects become "dynamic": Halide perovskites: A new window on materials? Mater. Horiz. **6**, 1297 (2019).

[33] Y. Shao, Y. Fang, T. Li, Q. Wang, Q. Dong, Y. Deng, Y. Yuan, H. Wei, M. Wang, A. Gruverman, J. Shield, and J. Huang, Grain boundary dominated ion migration in polycrystalline organic-inorganic halide perovskite films, Energy Environ. Sci. **9**, 1752 (2016).

[34] D. W. Ferdani, S. R. Pering, D. Ghosh, P. Kubiak, A. B. Walker, S. E. Lewis, A. L. Johnson, P. J. Baker, M. S. Islam, and P. J. Cameron, Partial cation substitution reduces iodide ion transport in lead iodide perovskite solar cells, Energy Environ. Sci. **12**, 2264 (2019).

[35] J. M. Frost and A. Walsh, What is moving in hybrid halide perovskite solar cells? Acc. Chem. Res. **49**, 528 (2016).

[36] T. Heiser and A. Mesli, Determination of the copper diffusion coefficient in silicon from transient ion-drift, Appl. Phys. A Solids Surf. **57**, 325 (1993).

[37] A. Zamouche, T. Heiser, and A. Mesli, Investigation of fast diffusing impurities in silicon by a transient ion drift method, Appl. Phys. Lett. **66**, 631 (1995).

[38] D. V. Lang, Deep-level transient spectroscopy: A new method to characterize traps in semiconductors, J. Appl. Phys. **45**, 3023 (1974).

[39] A. Khan and Y. Masafumi, in *Solar Cells—New Approaches and Reviews*, edited by L. A. Kosyachenko (InTech, Chernivtsi, 2015), Chap. 7.

[40] D. Abou-Ras, T. Kirchartz, and U. Rau, eds., *Advanced Characterization Techniques for Thin Film Solar Cells* (Wiley-VCH Verlag GmbH & Co. KGaA, Weinheim, 2016), Chap. 3.

[41] See the Supplemental Material at http://link.aps.org/supplemental/10.1103/PhysRevApplied.13.034018 for further information about the investigated solar cells, the validation of REGSLAPS, and further measurements with different DLTS modes.

[42] C. Tin, *Characterization of Materials*, edited by E. N. Kaufmann (John Wiley & Sons, Inc., Auburn, 2002), Chap. 5, p. 418.

[43] D. K. Schroder, *Semiconductor Material and Device Characterization* (John Wiley & Sons, Inc., Tempe, 2005).

[44] S. W. Provencher, A constrained regularization method for inverting data represented by linear algebraic or integral equations, Comput. Phys. Commun. **27**, 213 (1982).

[45] J. Weese, A reliable and fast method for the solution of Fredhol integral equations of the first kind based on Tikhonov regularization, Comput. Phys. Commun. **69**, 99 (1992).

[46] J. Weese, A regularization method for nonlinear ill-posed problems, Comput. Phys. Commun. **77**, 429 (1993).

[47] J. Honerkamp and J. Weese, Tikhonovs regularization method for ill-posed problems, Continuum Mech. Thermodyn. **2**, 17 (1990).

[48] L. Dobaczewski, A. R. Peaker, and K. B. Nielsen, Laplace-transform deep-level spectroscopy: The technique and its applications to the study of point defects in semiconductors, J. Appl. Phys. **96**, 4689 (2004).

[49] H. W. Engl, M. Hanke, and A. Neubauer, *Regularization of Inverse Problems*, Mathematics and Its Applications (Kluwer Academic Publishers, Dordrecht, 1996).

[50] I. Daubechies, M. Defrise, and C. De Mol, An iterative thresholding algorithm for linear inverse problems with a sparsity constraint, Commun. Pure. Appl. Math. **57**, 1413 (2004).

[51] A. Beck and M. Teboulle, A fast iterative shrinkage-thresholding algorithm for linear inverse problems, SIAM J. Imaging Sci. **2**, 183 (2009).

[52] V. A. Morozow, On the solution of functional equations by the method of regularization, Soviet Math. Dokl. **7**, 414 (1966).

[53] H. J. Snaith, A. Abate, J. M. Ball, G. E. Eperon, T. Leijtens, N. K. Noel, S. D. Stranks, J. T.-W. Wang, K. Wojciechowski, and W. Zhang, Anomalous hysteresis in perovskite solar cells, J. Phys. Chem. Lett. **5**, 1511 (2014).

[54] W. Tress, N. Marinova, T. Moehl, S. M. Zakeeruddin, M. K. Nazeeruddin, and M. Grätzel, Understanding the rate-dependent *J-V* hysteresis, slow time component, and aging in $CH_3NH_3PbI_3$ perovskite solar cells: The role of a compensated electric field, Energy Environ. Sci. **8**, 995 (2015).

[55] E. L. Unger, E. T. Hoke, C. D. Bailie, W. H. Nguyen, A. R. Bowring, T. Heumüller, M. G. Christoforo, and M. D. McGehee, Hysteresis and transient behavior in current-voltage measurements of hybrid-perovskite absorber solar cells, Energy Environ. Sci. **7**, 3690 (2014).

[56] L. Contreras, J. Idıgoras, A. Todinova, M. Salado, S. Kazim, S. Ahmad, and J. A. Anta, Specific cation interactions as the cause of slow dynamics and hysteresis in dye and perovskite solar cells: A small-perturbation study, Phys. Chem. Chem. Phys. **18**, 31033 (2016).

[57] S. A. L. Weber, I. M. Hermes, S.-H. Turren-Cruz, C. Gort, V. W. Bergmann, L. Gilson, A. Hagfeldt, M. Graetzel, W. Tress, and R. Berger, How the formation of interfacial charge causes hysteresis in perovskite solar cells, Energy Environ. Sci. **11**, 2404 (2018).

[58] J.-W. Lee, S.-G. Kim, J.-M. Yang, Y. Yang, and N.-G. Park, Verification and mitigation of ion migration in perovskite solar cells, APL Mater. **7**, 041111 (2019).

[59] G. Y. Kim, A. Senocrate, T.-Y. Yang, G. Gregori, M. Grätzel, and J. Maier, Large tunable photoeffect on ion conduction in halide perovskites and implications for photodecomposition, Nat. Mater. **17**, 445 (2018).

[60] P. Calado, A. M. Telford, D. Bryant, X. Li, J. Nelson, B. C. O'Regan, and P. R. Barnes, Evidence for ion migration in hybrid perovskite solar cells with minimal hysteresis, Nat. Commun. **7**, 13831 (2016).

[61] W. A. Saidi and J. J. Choi, Nature of the cubic to tetragonal phase transition in methylammonium lead iodide perovskite, J. Chem. Phys. **145**, 144702 (2016).

[62] G. P. Li and K. L. Wang, A novel technique for studying electric field effect of carrier emission from a deep level center, Appl. Phys. Lett. **42**, 838 (1983).

[63] G. P. Li and K. L. Wang, Detection sensitivity and spatial resolution of reverse-bias pulsed deep-level transient spectroscopy for studying electric field-enhanced carrier emission, J. Appl. Phys. **57**, 1016 (1985).

[64] M. Fischer, K. Tvingstedt, A. Baumann, and V. Dyakonov, Doping profile in planar hybrid perovskite solar cells identifying mobile ions, ACS Appl. Energy Mater. **1**, 5129 (2018).

[65] T.-Y. Yang, G. Gregori, N. Pellet, M. Grätzel, and J. Maier, The significance of ion conduction in a hybrid organic-inorganic lead-iodide-based perovskite photosensitizer, Angew. Chem. Int. Ed. **54**, 7905 (2015).

[66] A. Musiienko, P. Moravec, R. Grill, P. Praus, I. Vasylchenko, J. Pekarek, J. Tisdale, K. Ridzonova, E. Belas, L. Landová, B. Hu, E. Lukosi, and M. Ahmadi, Deep levels, charge transport and mixed conductivity in organometallic halide perovskites, Energy Environ. Sci. **12**, 1413 (2019).

[67] W. S. Yang, B.-W. Park, E. H. Jung, N. J. Jeon, Y. C. Kim, D. U. Lee, S. S. Shin, J. Seo, E. K. Kim, J. H. Noh, and S. I. Seok, Iodide management in formamidinium-lead-halide–based perovskite layers for efficient solar cells, Science **356**, 1376 (2017).

[68] P. Fassl, S. Ternes, V. Lami, Y. Zakharko, D. Heimfarth, P. E. Hopkinson, F. Paulus, A. D. Taylor, J. Zaumseil, and Y. Vaynzof, Effect of crystal grain orientation on the rate of ionic transport in perovskite polycrystalline thin films, ACS Appl. Mater. Interfaces **11**, 2490 (2018).

[69] E. Guillén, F. J. Ramos, J. A. Anta, and S. Ahmad, Elucidating transport-recombination mechanisms in perovskite solar cells by small-perturbation techniques, J. Phys. Chem. C **118**, 22913 (2014).

[70] A. Pockett and M. J. Carnie, Ionic influences on recombination in perovskite solar cells, ACS Energy Lett. **2**, 683 (2017).

[71] F. Ebadi, M. Aryanpour, R. Mohammadpour, and N. Taghavinia, Coupled ionic-electronic equivalent circuit to describe asymmetric rise and decay of photovoltage profile in perovskite solar cells, Sci. Rep. **9**, 11962 (2019).

[72] S. Ravishankar, A. Riquelme, S. K. Sarkar, M. Garcia-Batlle, G. Garcia-Belmonte, and J. Bisquert, Intensity-modulated photocurrent spectroscopy and its application to perovskite solar cells, J. Phys. Chem. C **123**, 24995 (2019).